Research Article Vol. 33, No. 1 / 13 Jan 2025 / Optics Express 1
Optics EXPRESS

Linear field-resolved spectroscopy approaching ultimate detection sensitivity

CHRISTINA HOFER,[1,2,3,4,†] DANIEL BAUSCH,[1,2,5,†] LUKAS FÜRST,[1,6] ZHENG WEI,[1,2] MAXIMILIAN HÖGNER,[1,2,7] THOMAS PATRICK BUTLER,[2] MARTIN GEBHARDT,[8,9,10,11] TOBIAS HEUERMANN,[8,9,10] CHRISTIAN GAIDA,[12] KIRAN SANKAR MAITI,[2] MARINUS HUBER,[1,2] ERNST FILL,[2] JENS LIMPERT,[8,9,10,12] FERENC KRAUSZ,[1,2,3] NICHOLAS KARPOWICZ,[1,2] AND IOACHIM PUPEZA[1,2,5,7,*]

[1]*Ludwig-Maximilians-Universität München, Am Coulombwall 1, 85748 Garching, Germany*
[2]*Max Planck Institute of Quantum Optics, Hans-Kopfermann-Str. 1, 85748 Garching, Germany*
[3]*Center for Molecular Fingerprinting, Molekuláris-Ujjlenyomat Kutató Közhasznú Nonprofit Kft., Budapest, Hungary*
[4]*Currently with: Quantum Matter Institute, University of British Columbia, 2355 East Mall, Vancouver, British Columbia V6T 1Z4, Canada*
[5]*Leibniz Institute of Photonic Technology, "Leibniz Health Technologies", Jena, Germany*
[6]*Currently with: Institute of Experimental Physics, Graz University of Technology, Graz, Austria*
[7]*Rheinland-Pfälzische Technische Universität Kaiserslautern-Landau, Kaiserslautern, Germany*
[8]*Institute of Applied Physics, Abbe Centre of Photonics, Friedrich Schiller University Jena, Germany*
[9]*Helmholtz-Institute Jena, Germany*
[10]*Gesellschaft für Schwerionenforschung, Darmstadt, Germany*
[11]*Currently with: School of Engineering and Physical Sciences, Heriot-Watt University, Edinburgh, Scotland, United Kingdom*
[12]*Active Fibre Systems GmbH, Jena, Germany*
[†]These authors contributed equally to this work.
[*]*ioachim.pupeza@rptu.de*

Abstract: Electric-field oscillations are now experimentally accessible in the THz-to-PHz frequency range. Their measurement delivers the most comprehensive information content attainable by optical spectroscopy – if performed with high sensitivity. Yet, the trade-off between bandwidth and efficiency associated with the nonlinear mixing necessary for field sampling has so far strongly restricted sensitivity in applications such as field-resolved spectroscopy of molecular vibrations. Here, we demonstrate electric-field sampling of octave-spanning mid-infrared waves in the 18-to-39 THz (600-to-1300 cm^{-1}) spectral region, with amplitudes ranging from the MV/cm level down to a few mV/cm. We show that employing powerful 2-µm gate pulses is key to approaching the ultimate detection limit of capturing all photons in the temporal gate, as well as providing high linearity with respect to the detected mid-infrared field. This combination of detection sensitivity, dynamic range, and linearity enables the exploitation of the full potential of emerging high-power waveform-controlled infrared sources for (non-)linear spectroscopy of solids, liquids, and gases.

1. Introduction

Recent progress in the generation of coherent mid-infrared (MIR) pulses resulted in table-top, waveform-stable sources with Watt-level average powers [1–3] and broad spectral coverage [4–8].

#536543 https://doi.org/10.1364/OE.536543
Journal © 2025 Received 26 Jul 2024; revised 15 Nov 2024; accepted 29 Nov 2024; published 2 Jan 2025

Optics EXPRESS

The temporal coherence of these sources enables field-resolved detection [9] and thus offers a vast new potential for the investigation of a wide range of dynamics in solids [10–13] and molecules [14–16] on the level of the electric field.

Among field-sensitive measurement techniques for mid-infrared pulses, electro-optic sampling (EOS) [17–19] stands out with respect to its sensitivity and dynamic range. In this spectral range, EOS is well described as a two-step process [20]: In the first step, an ultrashort gate pulse spectrally shifts the wave to be detected to shorter wavelengths, usually via sum- and/or difference-frequency generation. Secondly, the same gate pulse acts as a local oscillator for heterodyne detection. Among other examples, the sensitivity and sub-cycle temporal resolution of EOS has been essential in the direct detection of vacuum fluctuations [21]. Furthermore, the method has recently proven a power and bandwidth scalability [14,15] superior to traditional, time-integrating spectroscopies [22–25]. Quantitative MIR vibrational spectroscopy experiments employing EOS afford the most sensitive broadband infrared spectroscopy of biological systems to date [14] and dual-frequency-comb spectroscopy over the entire molecular fingerprint region [15,26,27].

While these represent breakthrough results, the nonlinear gating mechanism in EOS inherently limits the conversion efficiency of photons within the gating window to measurable photoelectrons in the detection electronics. For the quantification of the latter, we introduce the *effective quantum efficiency,* $QE_{\mathrm{eff}}(\nu)$*,* where ν denotes the MIR frequency. The quantity $QE_{\mathrm{eff}}(\nu)$ describes the MIR-frequency-resolved EOS response, it is determined by the gate pulse, the EOS crystal, and the subsequent optical arrangement. It is thus independent of the MIR test wave, of a specific gate-pulse delay and of the length of the sampled time window. The effective quantum efficiency in EOS can be treated and used analogously to the quantum efficiency of a conventional photodetector. For a test wave with a given spectro-temporal distribution and a total number of MIR photons $N_{\mathrm{ph}}(\tau)$ impinging onto the EOS detection within the temporal gate at a specific delay τ, $QE_{\mathrm{eff}}(\nu)$ determines the total number $N_{\mathrm{el}}(\tau)$ of MIR photons that are converted to photoelectrons. We refer to $N_{\mathrm{el}}(\tau)/N_{\mathrm{ph}}(\tau)$ as the *instantaneous quantum efficiency* $QE_{\mathrm{inst}}(\tau)$. Thus, while $QE_{\mathrm{eff}}(\nu)$ is independent of the MIR test wave, in general $QE_{\mathrm{inst}}(\tau)$ depends on the spectro-temporal evolution of the test wave, on the delay between gate and test pulse, and on $QE_{\mathrm{eff}}(\nu)$.

Until now, the instantaneous quantum efficiency of EOS has stayed well below 1%. In Ref. [28], the authors state an upconversion efficiency of 0.1% as an upper limit. From the parameters stated in Ref. [15], we estimate a $QE_{\mathrm{inst}}(\tau)$ of 0.013% in that work (see Appendix, section A.1). So far, to the best of our knowledge, the record $QE_{\mathrm{inst}}(\tau)$ was reported in Ref. [14], achieved with a 500-µm-thick GaSe EOS crystal – amounting to 0.5% for an EOS measurement in the 970-to-1320-cm^{-1} band (at -30 dB intensity) and resulting in a minimum detectable field strength of 26 mV/cm (calculated for a single temporal element and 1 s integration, see calculations in Appendix, section A.2).

Here, by employing powerful 2-µm gate pulses, we demonstrate electric-field sampling with an instantaneous quantum efficiency of 7.9%, an effective quantum efficiency with a maximum of 17% (at 1067 cm^{-1}) and an average of 4.3% throughout the 600-to-1300-cm^{-1} spectral region. This exceeds the previous record for broadband spectroscopy in the MIR range [14] by more than one order of magnitude while simultaneously doubling the detection bandwidth. In this MIR photon upconversion picture of EOS, the field measurement sensitivity lies within a factor of 4 from the ultimate limit of detecting all photons in the interaction time window of the gate pulse with the MIR wave. At the same time, the high gate-pulse energy affords a high degree of linearity for the measurement of MIR fields, with strengths ranging from a few mV/cm to the MV/cm level, that is, over more than 15 orders of magnitude in intensity.

Optics EXPRESS

2. Experimental concept

Drawing on preliminary experiments [1,29], we implemented EOS of a 50-MHz-repetition-rate train of few-cycle MIR waveforms, with 1.9-W-average-power, 13.8-fs gate pulses spectrally centred at 1.95 µm, using GaSe nonlinear crystals (Fig. 1 (a), for detailed setup description see Appendix, section A.3).

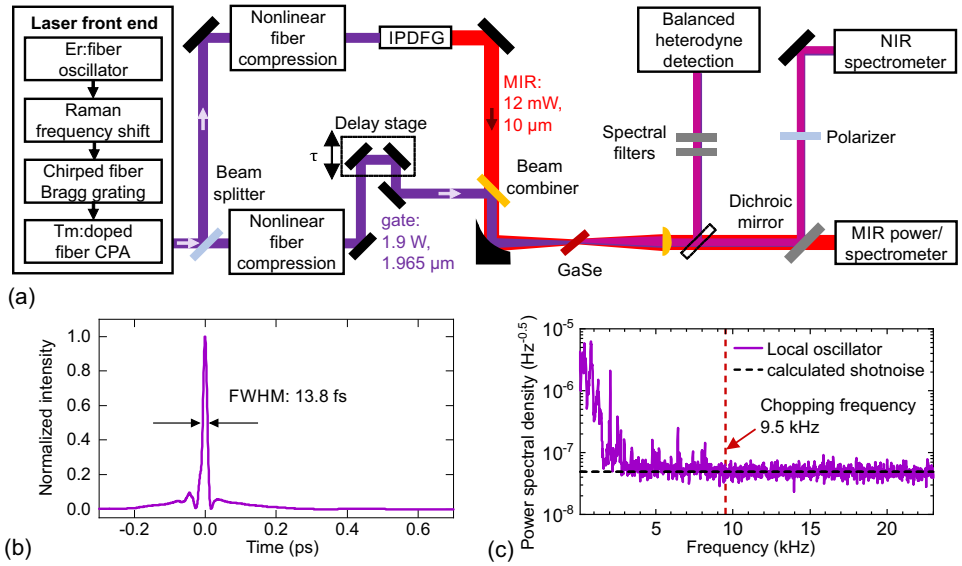

Fig. 1. Schematic of the experimental setup. (a) Measurement of the photon detection efficiency (without the dashed-line-framed mirror): Intra-pulse difference frequency generation (IPDFG) generates a 50-MHz-train of waveform-stable, few-cycle mid-infrared (MIR) pulses. This pulse train is focused collinearly with the variably-delayed (τ) train of 2-µm gate pulses (panel (b)) onto the EOS crystal (GaSe). The spectrally-integrated MIR average power and the gate pulse spectrum are recorded as functions of τ. Coherent field oscillations are sampled electro-optically using the variably-delayed 2-µm gate pulses and a balanced heterodyne detection setup including spectral filters [28]. (c) Frequency-resolved noise of the local-oscillator balanced-detection signal. Its power spectral density (PSD) (MIR beam blocked) was measured after minimizing the noise with the waveplates before the Wollaston prism. The detection noise at the lock-in frequency of 9.5 kHz reaches the single-sided power spectral density of the shot noise, calculated [46] from the average power impinging on the diodes (~0.4 mW) and the central wavelength (1550 nm).

In contrast to EOS configured for simultaneous sum- and difference-frequency generation, which requires a thin crystal [30], here we maximized the $QE_{\mathrm{inst}}(\tau)$ of phase-matched EOS using sum-frequency generation [14,31,32]. To this end, both the carrier wavelength and the average power of the gate pulses were increased as compared to the most sensitive EOS implementations to date [14,21]. The long central wavelength favours increasing the crystal thickness, which benefits the nonlinear conversion without compromising broadband detection [33]. In addition, the reduced gate-pulse photon energy mitigates multi-photon absorption, allowing for higher gate-pulse intensities (here: 9×10^{10} W/cm^2) inside the EOS crystal, maximizing the upconversion efficiency.

Optics EXPRESS

3. Results

3.1. High-sensitivity optical-field sampling

Scanning the gate pulse (temporal intensity envelope in Fig. 1(b)) over a delay range of 1.3 ps using a 541-µm-thick GaSe crystal as the EOS interaction medium resulted in the trace shown in red in Fig. 2(a) (time-dependent EOS-signal-to-detection-noise ratio, SDNR). For each of the 2240 data points (i.e., temporal elements), the integration time was 2.2 ms.

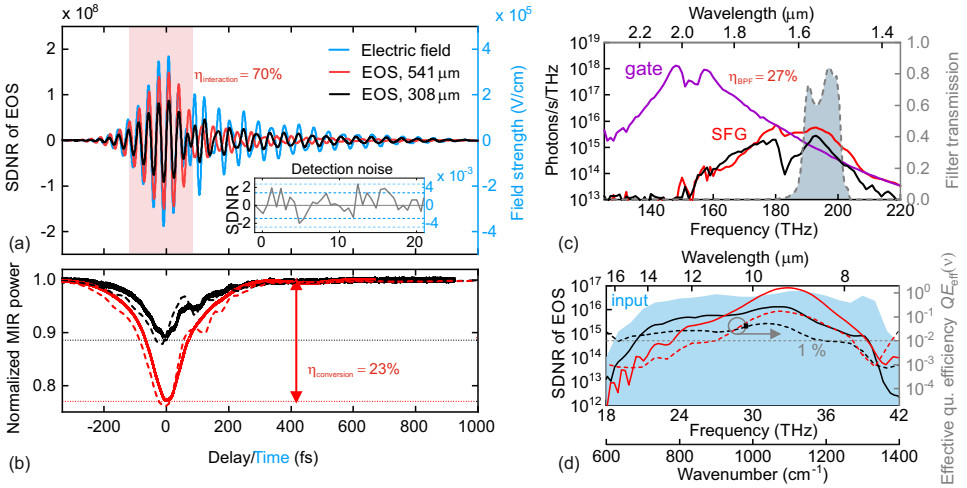

Fig. 2. EOS detection efficiency and dynamic range for two different detection crystal thicknesses. (a) Measured EOS trace with EOS-signal-to-detection-noise ratio SDNR (red, black) on the left y-axis. Blue on right y-axis: retrieved electric-field at the EOS crystal (see also Appendix, Fig. 8). Inset: detection noise measurement (blocked MIR, in grey). Dotted lines: minimum detectable field strength (to achieve SDNR = 1) for crystal thicknesses 308 µm in turquoise and 541 µm in blue. (b) Measured (solid) and simulated (dashed) spectrally-integrated MIR power behind the EOS crystal (see Fig. 1), using the same time axis as in (a), $\eta_{\text{conversion}}$: MIR-to-sum-frequency conversion efficiency measured at maximum depletion. (c) Sum-frequency signal (red, black) between MIR wave and gate pulses (purple, blocked MIR beam), recorded at maximum MIR depletion, and bandpass-filter transmission (grey area, η_{BPF}). (d) Blue area: MIR spectrum impinging on the EOS crystal (at arbitrary logarithmic scale), measured with a Fourier-transform spectrometer. Left y-axis/continuous line: EOS spectral-intensity SDNR obtained from the full scan shown in (a), scales linearly with measurement time [14]. Right y-axis/dashed line: effective quantum efficiency ($QE_{\text{eff}}(\nu)$, independent on measurement time). Grey dashed line indicates a $QE_{\text{eff}}(\nu)$ of 1%.

The detection noise floor (inset in Fig. 2(a) is dominated by the gate-pulse shot noise in the balanced detection [34] (Fig. 1(c)) and was measured for an integration time of 1 s per temporal element for comparison to the flux of MIR photons incident on the EOS detection crystal. Linear scaling of the intensity SDNR (and square root scaling for the SDNR of EOS) for integration times up to 1600 s was previously shown [14].

In the following, we estimate $QE_{\text{eff}}(\nu)$ (see Appendix, section A.4 for complete mathematical definitions) by considering, one by one, each step in the EOS process. First, we calculate $QE_{\text{inst}}(0)$ by estimating the number of generated photoelectrons $N_{\text{el}}(0)$ in relation to the number of incoming MIR photons within the temporal gate, $N_{\text{ph}}(0)$, at the delay of maximum absolute MIR power depletion ($\tau = 0$). The direct measurement of MIR depletion yields that 23% of all MIR photons were converted ($\eta_{\text{conversion}} = 23$ %, Fig. 2(b)) mostly by SFG, see the section

Optics EXPRESS

on the detection linearity. This value depends on the chromatic dispersion of the MIR wave and, in general, increases with better temporal compression, confining a larger fraction of all MIR photons to the temporal gate. Considering the length of the temporal gate and the intensity envelope of MIR pulse, we estimate that approximately 70% of all MIR photons interact with the gate pulse upon propagation through the crystal ($\eta_{\mathrm{interaction}}$, indicated by shaded area), resulting in a depletion of $\eta_{\mathrm{conversion}}/\eta_{\mathrm{interaction}}$ = 33 % within the temporal gate (see Appendix, Fig. 7).

Figure 2(c) shows the spectrum of the generated sum-frequency radiation signal (black). An independent measurement of this signal strength revealed that it matches the MIR depletion in terms of photon number, allowing to exclude significant impact of other possible (nonlinear) mechanisms reducing the number of MIR photons. The combination of spectral filters employed to optimize the SDNR [28] had an overall transmission η_{BPF} = 27 %. Selecting this spectral band for balanced heterodyne detection reduced the fraction of detectable MIR photons from within the temporal gate to $\eta_{\mathrm{conversion}}/\eta_{\mathrm{interaction}} \times \eta_{\mathrm{BPF}}$ = 8.9 %. Correcting this figure for the Fresnel losses at the entrance surface in the GaSe crystal (η_{Fresnel} = 88.5 %), and assuming unity quantum efficiency for the photodiodes results in a $QE_{\mathrm{inst}}(\tau)$ of 7.9%. Assuming a delay-independent spectral distribution of the MIR wave, the $QE_{\mathrm{inst}}(\tau)$ can now can be used to estimate the effective quantum efficiency $QE_{\mathrm{eff}}(\nu)$ by considering the photon spectral density of the incident MIR radiation and the measured spectrum as calculated from the EOS trace via a Fourier transform (Fig. 2(d), see also Appendix, Fig. 8). This assumption is important, as $\eta_{\mathrm{interaction}}$ would otherwise have both a spectral and a delay dependence.

The $QE_{\mathrm{eff}}(\nu)$ peaks at 17% and exceeds 1% in the 900-to-1270 cm^{-1} range. This high effective quantum efficiency, together with shot-noise-limited balanced detection (Fig. 1(c)), results in the measurement noise floor shown in the inset in Fig. 2(a), indicating a minimum detectable field strength of 2.7 mV/cm (dashed line) for a MIR beam radius of 35 µm at the 541-µm-thick detection crystal. For comparison, this value is only a factor of ~4 above the ultimate limit achievable with an ideal EOS detection capturing all MIR photons within the temporal gate.

The shape and duration of the temporal gate (see Appendix, Fig. 7) and, therefore, the temporal resolution (or, the detection bandwidth), as well as the upconversion efficiency, result from a complex interplay of the experimental parameters [20]. These include crystal thickness and orientation, gate-pulse power, bandwidth, and chirp, as well as focusing geometry and spectral filters. For instance, a more uniform spectral coverage at the expense of a lower detection efficiency was achieved employing a 308-µm-thick EOS crystal. In this case, the spectral range for η_{total}>1 % is increased by about a factor of 1.5 (640-1185 cm^{-1}, black lines in Fig. 2, Table 1).

Table 1. Comparison of the various efficiency values for two different thicknesses of GaSe crystals used as the nonlinear medium in the EOS detection

thickness GaSe [µm]	$\eta_{\mathrm{conversion}}$ [%]	$\eta_{\mathrm{interaction}}$ [%]	η_{BPF} [%]	η_{Fresnel} [%]	$QE_{\mathrm{inst}}(\tau)$ [%]	peak $QE_{\mathrm{eff}}(\nu)$ [%]	spectral range with $QE_{\mathrm{eff}}(\nu)$>1% [cm^{-1}]	E_{min} [mV/cm]
308	11	60	25	88.5	4.1	5.3	640-1185	4.7
541	23	70	27	88.5	7.9	17.3	900-1270	2.7

3.2. Detection linearity

In addition to sensitivity, linearity of detection is crucial for measurements involving electric fields with strongly varying strength. One example is the free-induction decay of solid, liquid or gaseous samples after strong, impulsive excitation. In EOS employing both sum- and difference frequency mixing, the two nonlinear effects approximately balance the MIR power loss and gain. As we only phase-match sum-frequency generation and drive this process very strongly, the MIR power is substantially depleted in our setting (cf. Figure 2(b)). This results in a dependence of the

Optics EXPRESS

total photocurrent at the balanced diodes on the MIR field strength. The normalized photocurrent $\Delta I/I$ – which is commonly used as the electro-optic signal in low-depletion EOS configurations to eliminate gate-pulse fluctuations (among others, in Refs. [21,30–32,35–37]) – would thus be strongly nonlinear. In the context of EOS of strong THz fields, this has been treated as an over-rotation caused by the Pockels effect [35,36].

Here, this is not critical as we measure the non-normalized differential current ΔI. In addition, the depletion of the interacting fields via second-order nonlinear conversion processes, as well as higher-order nonlinearities might constitute potential sources for deviations from an ideally-linear instrument response function. We numerically studied these deviations induced by second- and third-order nonlinear processes in the EOS crystal (see also Appendix, section A.5). We define the figures of merit dA and $d\varphi$ to quantify the detection nonlinearity for the temporal amplitude and phase, respectively, as elucidated in Fig. 3(a).

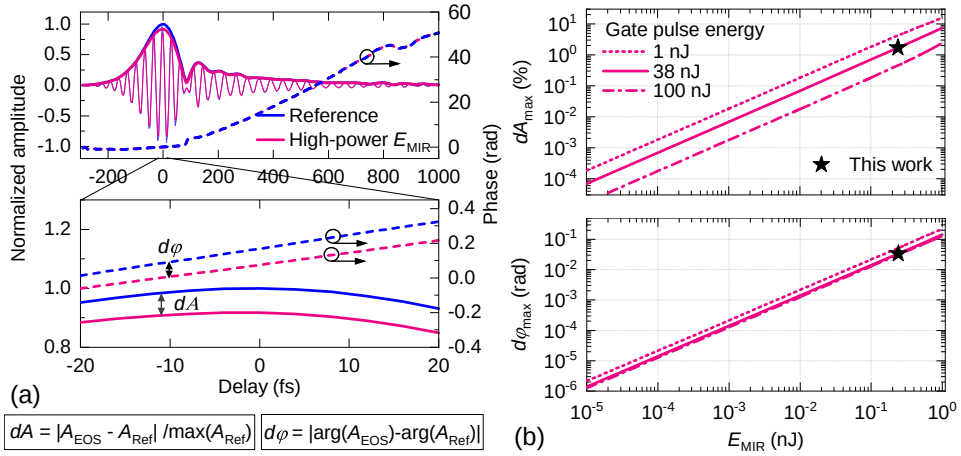

Fig. 3. Simulations of the detection linearity. (a) Figures of merit for the quantification of the EOS detection nonlinearity. The temporal, cycle-averaged envelope (left y-axis) and phase (right y-axis) are calculated from simulated EOS traces via Hilbert transformation for two MIR field strengths: a low-energy reference trace (blue), for which EOS linearity in the MIR field can be assumed, and an energy-scaled version of the same waveform (magenta). The amplitude of the reference field is normalized while the other field is scaled with the square root of the MIR power. (b) Figures of merit dA and $d\varphi$ obtained via numerical simulations of EOS for a large range of MIR-pulse energies (E_{MIR}, x-axis) and different gate-pulse energies (see legend).

Their maximum values determined for our model input field (see Appendix, Fig. 8) are plotted in Fig. 3(b) for a wide range of energies of the pulses interacting in the EOS crystal. For our experimental parameters, the study predicts maximum values for dA and $d\varphi$ on the order of 2% and 30 mrad, respectively, at a MIR field strength of 430 kV/cm, and values below 10^{-5}% and 2 µrad, respectively, for MIR field strengths lower than 1 kV/cm.

For an experimental verification of this degree of detection linearity, we attenuated the intensity of the MIR beam with optical-density (OD) filters by one order of magnitude (Fig. 4(a)). The insets illustrate that in comparison to the technical instrument drifts and signal strength fluctuations, the expected nonlinearity effects are negligible. For a further test of the detection sensitivity and linearity, we attenuated the MIR power by more than 13 orders of magnitude and plotted the intensity spectra and spectral phases for an average of 10 EOS traces each (Figs. 4(b) and (c)). This confirms measurable MIR powers from tens of mW to below the fW-level and the measurement linearity over this entire power range.

Optics EXPRESS

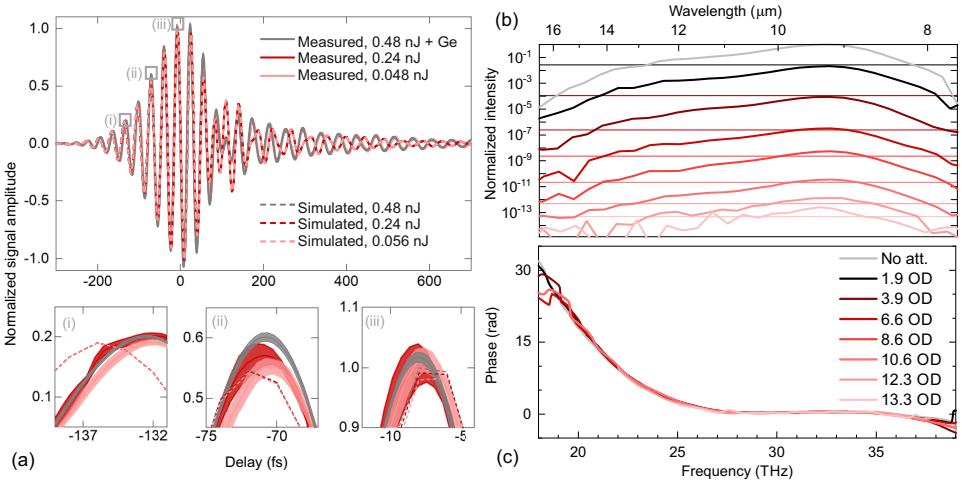

Fig. 4. Measurements of the detection linearity. (a) Measured (solid lines) and simulated (dashed lines) EOS traces for three different MIR pulse energies. Traces are normalized relative to each other with the square-root of the intensity attenuation factor. The measured EOS trace for no attenuation was numerically propagated through 1-mm-thick Ge. Zoom-ins serve to show variations of the trace maxima as a function of signal/MIR field strength. For the measured data, the lines represent the average of 10 measurements and the shaded areas the standard deviation. Note that the error corridor scales with the absolute trace amplitude. (b) Measured intensity spectra for an average of 10 EOS traces (2.2 ms integration time per temporal element) with varying attenuation of the MIR power (see legend in panel (c)). Spectra are normalized/scaled to the maximum of the spectrum with no attenuation, the measurement noise floor (blocked MIR beam) coincides with the x-axis. Horizontal lines indicate the peak of the spectrum expected from the nominal filter attenuation. (c) Spectral phases corresponding to the spectra in (b), scaled with a phase corresponding to a group delay to account for temporal shifts caused by the filters.

Figure 3(b) reveals an improvement of the detection linearity for higher gate-pulse energies. The numerical simulations (details in Appendix, section A.5) confirm that this finding can be explained by the depletion of the gate pulse upon interacting with the MIR field in the EOS crystal: Although the conversion of the MIR pulse increases with gate-pulse energy, the relative depletion of the gate pulse is smaller, in effect leading to a smaller deviation from a purely linear response. Consequently, we found that a large number of gate-pulse photons simultaneously benefits the detection sensitivity and the linearity of field-sensitive detection over a wide range of intensities.

In the following, we demonstrate that the linear detection capability across a large dynamic range of field strengths directly translates to a large dynamic range of concentration quantification in molecular vibrational spectroscopy. A widespread challenge in MIR sensing applications is that the employed spectrometer may be well suited for trace substance detection, but may saturate when measuring strong signals, or vice versa. Consequently, depending on the specific measurement task, it can become necessary to adjust either the spectrometer itself or the path length of the interaction with the sample, leading to a cumbersome process for measurements spanning a wide concentration range [38]. To illustrate the potential of field-resolved infrared spectroscopy to surmount this limitation, we conducted experiments measuring the transmission of MIR pulses through a 45-cm-long gas cell containing various concentrations of methanol. Figure 5(a) shows the envelope of the recorded time-domain EOS traces.

Optics EXPRESS

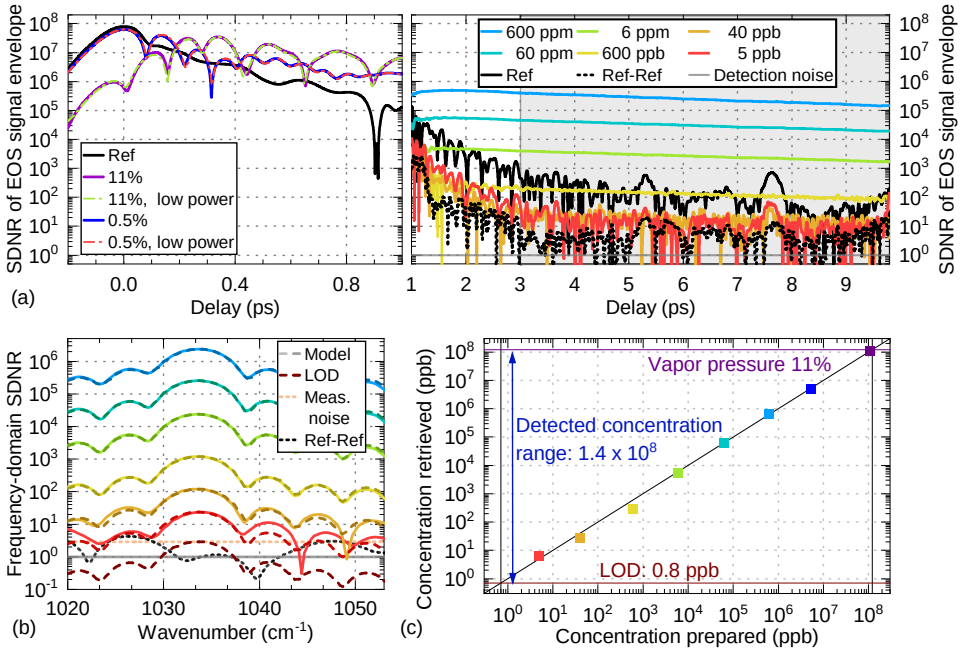

Fig. 5. Field-resolved spectroscopy of methanol. (a) Envelopes of time-domain EOS traces, normalized to the single-scan detection-noise level. Black line: reference waveform (evacuated gas cell). Left panel: reference and sample response for percent-level concentrations with excitation powers of 19 mW in a 6-mm $1/e^2$-intensity-diameter beam at the sample (12 mW reaching the EOS crystal, solid line) and ~100 times lower power (dashed lines). Right panel: differences between sample-response and empty-cell reference measurements (Ref.). Individual 10.6-ps-long traces were acquired in an effective total measurement time of 80 seconds per trace. (b) Solid: magnitude of the Fourier transforms of the signals in (a), in the 3-ps-to-9.8-ps time window. Dashed: HITRAN model. (c) Retrieved versus prepared concentration. See Appendix, section A.6 for details on sample preparation, signal acquisition, processing, and concentration retrieval.

Empty-cell EOS measurements allow for a quantitative comparison of the molecular response with the HITRAN line-by-line database [39,40], see also Appendix, section A.6. The reference measurement (that is, the difference of two empty-cell EOS traces, Fig. 5(a), black dotted line) shows that roughly 3 ps after the excitation maximum, detection-noise-limited sensitivity is approached within a factor of 3 (limited by residual MIR source noise). Evaluating the methanol Q-branch signal in the 3-ps-to-9.8-ps time window after subtraction of the separately-measured empty-cell response yields excellent agreement with the HITRAN-based model for concentrations below 1000 ppm (Fig. 5(b)). A noise-equivalent limit of detection (LOD) of 0.8 ppb is obtained (Fig. 5(b), brown line).

Near vapor pressure, strong modulations of the leading part of the sample response are observed. To ensure that these can be solely attributed to the linear refractive index of the sample, we measured the response of two high concentrations (0.5% and 11%) at a 100-times weaker excitation power (Fig. 5(a), left, dashed lines). The accordance of the respective sample responses confirms the linearity both of the light-matter interaction and of the instrument response within our measurement accuracy. Thus, linear detection of methanol over a range of concentrations spanning 8 orders of magnitude was confirmed (see Fig. 5(c)). A thorough study of the performance now coming into reach in MIR vibrational (gas-phase) spectroscopy exceeds

Optics EXPRESS

the scope of this paper. It is however worth mentioning, that the presented linear EOS detection, along with path-length elongation instrumentation such as multi-pass cells [41] or enhancement cavities [42–44], bring quantitative gas detection of concentrations in the lower (or even sub-) ppt range into reach.

4. Conclusion

In conclusion, we have demonstrated sampling of super-octave long-wave mid-infrared electric fields with sensitivities approaching the ultimate limit set by the detection of all infrared photons within the temporal gate. For our geometry, this implies the ability to measure MIR electric-field strengths in the few-mV/cm range, with detection linearity preserved up to the MV/cm field-strength range. Key to both the unprecedented combination of a detection with broad bandwidth and high sensitivity, and to the high degree of linearity was the use of high-power 2-µm gate pulses.

The experimentally-demonstrated upconversion efficiency, in combination with lower-noise gate pulses allowing for an increase of η_{BPF} would enable a peak detection efficiency exceeding 50% (see Appendix, section A.7). Geometric scaling of the EOS focus, while keeping the peak intensities of the interacting beams the same increases the effective interaction length by reducing the impact of spatial walk-off and extending the Rayleigh length. This promises peak upconversion efficiencies approaching 100% while preserving linearity in the MIR field strength (see Appendix, Fig. 10). For the QE_{inst} (τ), this would correspond to an increase by a factor of ~ 4.5, resulting in ~ 27%.

This new regime of detection sensitivity and dynamic range, together with its power scalability opens new perspectives for ultrafast optical spectroscopy. An example par excellence is quantitative, label-free breath gas analysis for identifying and monitoring infectious diseases [45] and cancer [46].

Appendix

A.1. Estimation of the instantaneous quantum efficiency in Ref. [15]

The authors claim a time-domain signal-to-noise ratio of 40, for a detection bandwidth of 50 MHz. With the stated MIR power of 50 µW and central frequency of 39 THz, this corresponds to 4×10^7 photons within the integration time window. Attenuation by $40^2 = 1600$ (to result in a SNR of 1) leads to 24000 photons within the integration time, and an estimated 8000 photons within the interaction time window (MIR pulse duration: 29 fs, gate pulse duration: 10 fs), corresponding to an $QE_{\mathrm{inst}}(\tau)$ of 0.013%.

A.2. Estimation of the minimum detectable field strength

The minimum detectable field strength is calculated according to the following formula:

$$E_{\min}\left[\frac{\mathrm{mV}}{\mathrm{cm}}\right] \approx \sqrt{\frac{4 \times P_{\mathrm{avg}}[\mathrm{W}]}{SNR_{1s}^2 \times f_{\mathrm{rep}}[\mathrm{Hz}] \times \tau_p[\mathrm{s}] \times w^2[\mathrm{cm}^2] \times \pi \times c\left[\frac{\mathrm{m}}{\mathrm{s}}\right] \times \epsilon_0\left[\frac{\mathrm{As}}{\mathrm{Vm}}\right]}}$$

This formula uses the relation between intensity I and electric-field strength E of a laser pulse: $I = \frac{c\epsilon_0 n}{2}|E|^2$, with $n \approx 1$, calculated for the peak intensity: $I_{\mathrm{peak}} \approx \frac{2 \times P_{\mathrm{avg}}}{f_{\mathrm{rep}} \times \tau_{\mathrm{p}} \times \pi \times w^2}$. An additional factor 2 for the average power results from the chopped MIR pulse train. Here, P_{avg} is the average MIR power in the GaSe crystal (with Fresnel losses of 11.5% for the p-polarized MIR beam entering the 34°-rotated crystal), $SNR_{1\mathrm{s}}$ the signal-to-noise-ratio for 1s integration time per data point/temporal element, f_{rep} the laser repetition rate, τ_{p} the FWHM MIR pulse duration and w the beam waist.

Optics EXPRESS

In Ref. [14], a lock-in time constant of 183 µs (internal knowledge) is used with a 6th order filter. The settling time of the lock-in detection to reach 99% signal strength (from the Zurich Instruments manual) was assumed to obtain an integration time of 2.2 ms for the noise floor of a single measurement of 5×10^{-13}. The signal-to-noise-ratio for the 500-µm-thick GaSe crystal and a chopped average power of 12 mW (internal knowledge) amounts to 1.4×10^6 for this integration time, or $SNR_{1s} = 2.9 \times 10^7$ (assuming scaling of the signal-to-noise-ratio with the square-root of the integration time). We assumed $\tau_p = 60$ fs, $f_{rep} = 28$ MHz, $w = 35$ µm. This results in a minimum detectable field strength (1 s integration time) of 26 mV/cm. In this work, $SNR_{1s} = 1.5 \times 10^8$ (see Fig. 2(a)). We calculate a minimum detectable field strength of 2.7 mV/cm for the 541-µm-thick GaSe crystal with $\tau_p = 100$ fs and $w = 35$ µm.

A.3. Experimental setup

The employed instrument is an adapted implementation of the system described in detail in Ref. [1]. The detailed setup is depicted in Fig. 6. The pulsed output of an erbium fibre oscillator (Menlo C-fibre), operating at a wavelength of 1.5 µm and a repetition rate of 100 MHz, is pulse-picked down to 50 MHz, amplified and shifted to 2 µm in a highly nonlinear fibre. A chirped fibre Bragg grating cuts out a spectrum around 1965nm resulting in stretched pulses with 500-ps pulse duration. This pulse train seeds a two-stage thulium-doped fibre amplifier and delivers, after a free-space grating compressor, 2-µm pulses with a full-width-at-half-intensity maximum (FWHM) duration of 250 fs. Starting at the grating compressor, the free-space beam path is enclosed in a vacuum chamber ($<10^{-3}$ mbar) to avoid absorption from gases such as water vapor. The beam is split in two and the pulses are further compressed in silica photonic crystal fibres. Gate pulses for electro-optic sampling (EOS) are nonlinearly self-compressed in a large mode area fibre (LMA15 from NKT Photonics) down to a FWHM duration of 13.8 fs with an average power of 4.5 W. For mid-infrared (MIR) generation, the 2-µm pulses are compressed down to durations of 32 fs FWHM with 30 W of average power in a large-pitch-fibre (LPF40 fibre). Intra-pulse difference frequency generation (IPDFG) in a 1-mm-thick gallium selenide (GaSe) crystal results in waveform-stable MIR pulses with 250 mW average power and an intensity spectral coverage between 630 cm^{-1} and 1370 cm^{-1} at the -20-dB-level. As compared to the original implementation in Ref. [1], here we operate the system at a safe level below its power record. Grating-based long pass filters (LPF) separate the MIR pulses from the pump [47] before the MIR beam is mechanically chopped at a frequency of 10 kHz. The MIR beam passes the 45-cm-long gas cell with two 1-mm-thick ZnSe windows and a 10-mm-thick germanium substrate for second-order dispersion compensation. A 1-mm-thick ZnSe substrate placed at Brewster's angle recombines the gate (s-polarization, in reflection) and the MIR pulses (p-polarization, in transmission). The gate beam is transverse-mode-matched to the MIR beam via a reflective telescope employing curved mirrors. It is variably delayed for EOS measurements with a mechanical stage, whose displacement is tracked with a Michelson interferometer (Picoscale PS-CTRL-V1.3-TAB with C01 sensor head, SmarAct) . The collinearly propagating beams are focused into a GaSe crystal with average powers of 1.9 W and 12 mW for the gate and MIR pulses, respectively. The EOS crystal phase-matches p-polarized sum frequency generation (SFG). After a 1500-1600 nm bandpass filter, the 2-µm beam is split into two orthogonal polarizations by a Wollaston prism, followed by a custom-made balanced detector with two InGaAs diodes (G12180-005A, Hamamatsu). By adjusting a quarter-wave plate and a half-wave plate before the Wollaston prism, close to shot-noise-limited detection is achieved at the chopping frequency of 9.5 kHz. The balanced photocurrent is amplified (transimpedance amplifier DLPCA-200, FEMTO) and detected with a lock-in amplifier (MFLI, Zurich Instruments) and analog-to-digital converter (Picoscale Breakout Box PS-BOB-V1.0-TAB, SmarAct), using an integration time of 2.2 ms.

Optics EXPRESS

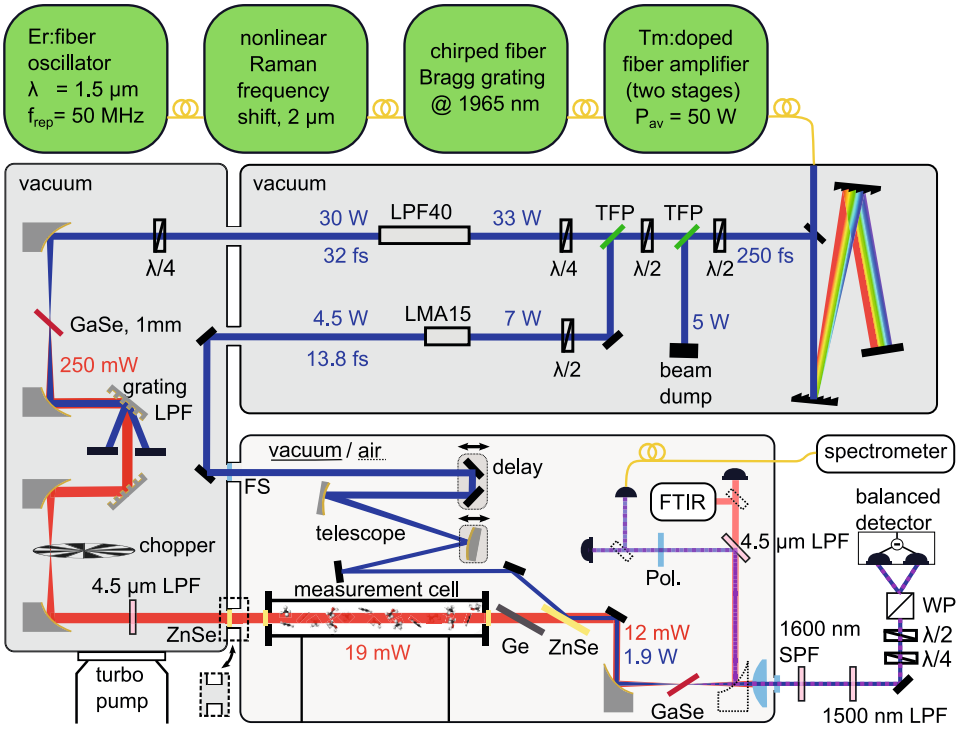

Fig. 6. Detailed schematic of the optical setup. Er: erbium, Tm: thulium, TFP: thin-film polarizer, LMA15: a large mode area fibre, LPF40: a large-pitch fibre, λ/2: half-wave plate, λ/4: quarter-wave plate, GaSe: gallium selenide, LPF: long-pass filter, FS: fused silica, ZnSe: zinc selenide, Ge: germanium, SPF: short-pass filter, WP: Wollaston prism. The detection efficiency measurements were performed with the last chamber in air, the ZnSe window between the chambers and the parabola after the EOS crystal inserted.

A.4. Estimation of the effective quantum efficiency in electro-optic sampling

The effective quantum efficiency $QE_{\mathrm{eff}}(\nu)$ displayed in Fig. 2(d) is calculated as follows: First, at the delay of maximum MIR depletion ($\tau = 0$), we calculate the instantaneous quantum efficiency $QE_{\mathrm{inst}}(0)$ as the ratio of generated photoelectrons to the number of MIR photons within the gate as $N_{\mathrm{el}}/N_{\mathrm{ph}} = \eta_{\mathrm{conversion}}/\eta_{\mathrm{interaction}} \times \eta_{\mathrm{BPF}} \times \eta_{\mathrm{Fresnel}}$ (see main text). Next, the area under the retrieved EOS spectrum is normalized to $N_{\mathrm{tot}} \times QE_{\mathrm{inst}}(0)$ in order to obtain the power spectral density $PSD_{\mathrm{EOS}}(\nu)$ as seen by the EOS detection, with N_{tot} being the total number of MIR photons incident on the EOS crystal per time. Finally, the ratio between $PSD_{\mathrm{EOS}}(\nu)$ and the input power spectral density $PSD_{\mathrm{FTIR}}(\nu)$ (obtained via an input power measurement with Fresnel losses at the GaSe interface of $\eta_{\mathrm{Fresnel}} = 88.5$ % and the independently, FTIR-measured spectrum) results in frequency-resolved gated efficiency $QE_{\mathrm{eff}}(\nu)$:

$$QE_{\mathrm{eff}}(\nu) = \frac{PSD_{\mathrm{EOS}}(\nu)}{PSD_{\mathrm{FTIR}}(\nu)}$$

Note, that this estimation neglects residual chirp of the MIR waveform, as it assumes a delay-independet spectral distribution equal to that of the FTIR spectrum and, correspondingly, a constant spectrally-integrated relative depletion throughout the entire EOS trace.

For validation, we relate the time-domain SDNR to the $QE_{\mathrm{inst}}(0)$. First, we calculate the MIR photon rate as a function of time (i.e., delay) from the MIR pulse energy and electric field distribution. For the given time-domain instrument response, the photons in the interaction time window at the delay of maximum signal strength are then estimated via integration of the

Optics EXPRESS

photon rate over the width of the interaction time window ($\eta_{\text{interaction}}$, see Fig. 7). The ratio of the SDNR to the photon rate then yields $QE_{\text{inst}}(0)$. This includes effects which are not considered by the calculation of MIR depletion and spectral filtering, e.g., spectrally varying phase relations between the sum-frequency and local oscillator components [30], as well as imperfect spatial interference. The result is an estimated $QE_{\text{inst}}(0)$ of 5.9%, which agrees well with the 7.9% stated in the main text, where less effects are considered.

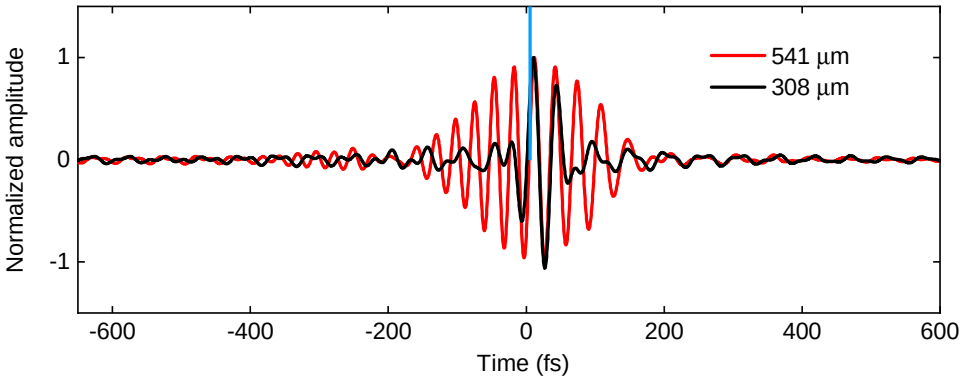

Fig. 7. Temporal gate functions for the two detection crystal thicknesses, calculated as the Fourier transform of the respective complex spectral instrument response (complex ratio of the Fourier transforms of the incident field (Fig. 8) and the EOS traces (Fig. 2(a))). Multiplication by the complex frequency-domain instrument response corresponds to a convolution of the incident electric field with this (oscillating) time-domain gate function. The blue peak indicates the Dirac-delta-peak-like temporal response required for the theoretical limit of measuring exactly the electric field. For the estimation of the number of photons interacting with the mid-infrared wave within the temporal gate, we integrate over the MIR photon rate over the FWHM of this time-domain response. $\eta_{\text{interaction}}$ is then calculated as the ratio of interacting photons to the total number of MIR photons per pulse, at the delay of maximum signal strength, i.e., where the gate pulse interacts with most photons.

Table 1 summarizes the detection efficiency and minimum detectable field strength for two different detection crystal thicknesses.

A.5. Numerical study of the EOS linearity

The linearity characteristics of the implemented EOS setup were studied with a simulation code based on the CUDA computing platform, implementing the nonlinear wave equation in the slowly varying wave approximation and considering 2^{nd} and 3^{rd} order nonlinear processes [48]. EOS traces were simulated using the experimental parameters (gate-pulse energy of 38 nJ, MIR-pulse energy of 0.24 nJ, 35-µm-beam waists; 541-µm-thick GaSe crystal) as well as the material parameters of GaSe (Sellmeier coefficients [49]; 2^{nd} and 3^{rd} order nonlinear coefficients [50,51]). The instrument response function was calculated with the gate-pulse intensity envelope shown in Fig. 1(b) (from second-harmonic generation frequency-resolved optical gating measurement), the crystal geometry as determined from the experimental setup ($\Theta = 34°$, $\varphi = 0°$) and the measured transmission for the 1500-1600-nm band-pass filter (Fig. 2(c), right). The input MIR electric field in Fig. 8 was estimated using the instrument response function for a measurement with a 130-µm-thick GaSe crystal, which ensured a well-behaved spectral response.

This calculated instrument response function incorporates phase matching, temporal and spatial walk-off, the gate-pulse properties and the effects of spectral filtering. It does not include spatial mismatch in the heterodyne detection and gives no information on the carrier-envelope phase of the MIR waveform [30] (which is irrelevant for the experiments shown here).

Optics EXPRESS

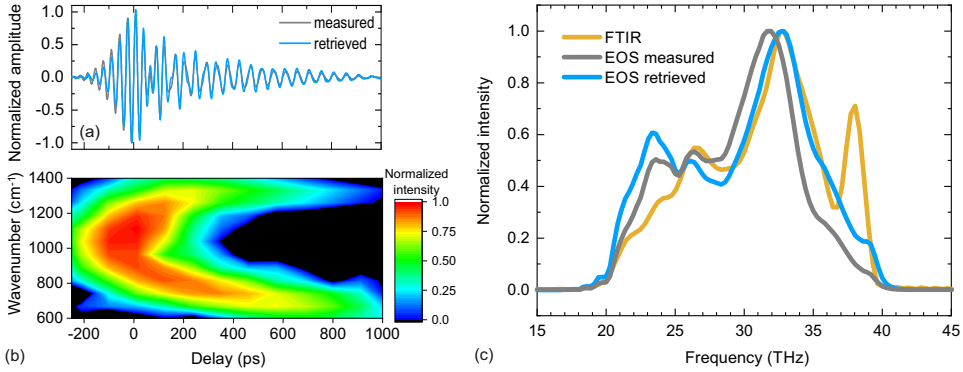

Fig. 8. Calculated MIR electric field and EOS instrument response function for a 130-µm-thick GaSe crystal, ensuring a broadband spectral response and negligible spatial walk-off (compare Fig. 7). (a) Measured EOS trace (grey), estimated MIR field (blue) retrieved using the calculated spectral response. (b) Spectrogram of the MIR waveform, elucidating the remaining chirp of this waveform. The time-dependent amplitude of the EOS trace results from a combination of the frequency-dependent detection efficiency and instantaneous spectrum. For thicker crystals it thus decreases towards longer delays in comparison to the MIR waveform (Fig. 2(a)), where the chirp is combined with the reduced detection efficiency for longer MIR wavelengths (Fig. 2(d)). (c) Measured (grey) and instrument-response-corrected (blue) MIR spectra, as well as MIR spectrum measured with a Fourier-transform infrared (FTIR) spectrometer (orange).

The Fourier transform of the measured trace was then divided by the simulated complex frequency-domain instrument response, yielding the estimation of the MIR field incident on the GaSe crystal. The simulations were validated by comparing the maximum power depletion of the MIR pulse after the 541-µm-thick GaSe crystal. The simulated 23% are consistent with the measured value of 23% (see Fig. 2(b)).

In the study of the detection linearity, the MIR-pulse and gate-pulse energies were varied over wide ranges (10^{-8} nJ to 1 nJ, and 1 nJ ~ 100 nJ, respectively) and the simulated EOS traces were normalized with the square root of the MIR field energies, respectively. For each gate-pulse energy, the respective EOS trace with 10^{-8}-nJ MIR-pulse energy was used as a reference, because the gate pulse is negligibly depleted in this case. The relative-amplitude difference of the envelopes dA and of the absolute temporal phase differences $d\varphi$ of the EOS traces are chosen as metrics for the EOS linearity, and are defined as: $dA = \frac{|A_{\mathrm{EOS}} - A_{\mathrm{Ref}}|}{\max(|A_{\mathrm{Ref}}|)}$ and $\mathrm{d}\varphi = |arg(A_{\mathrm{EOS}}) - arg(A_{\mathrm{Ref}})|$, where A_{EOS} and A_{Ref} are the complex envelopes of the EOS traces scaled by the square-root of the MIR pulse energies and the traces of the references, respectively. We denote their maxima as a function of delay as $dA_{\max}$ and $d\varphi_{\max}$. In order to investigate the source of the nonlinearity, simulations with the different susceptibilities of GaSe were performed. The depletion of the gate and MIR powers as well as the values for dA and $d\varphi$ are shown in Fig. 9. The impact of the third-order susceptibility was probed by setting $\chi^{(3)}$ to zero. The values for dA and $d\varphi$ with and without $\chi^{(3)}$ differ by less than 2%, implying that it plays a minor role in our experimental setting.

Furthermore, in a thought experiment, $\chi^{(2)}$ was doubled and the gate pulse energy was reduced by a factor of four to keep the MIR depletion constant, according to the scaling laws of a second-order nonlinear process. The geometry was maintained in the two cases. This resulted not only in a fourfold increase of the gate-pulse depletion, but also in more than threefold higher dA and $d\varphi$. This confirms that the depletion of the gate-pulse energy is the major cause for the nonlinearities.

Optics EXPRESS

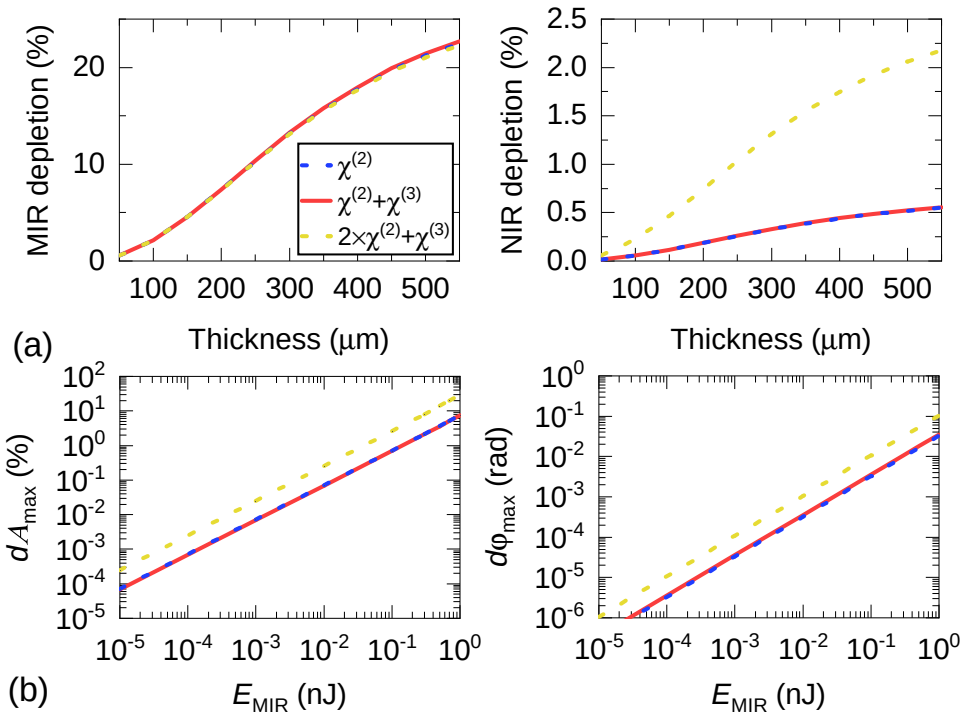

Fig. 9. Simulations of the EOS detection for different susceptibilities, and similar MIR conversion efficiencies. (a) Relative depletion of the MIR- and gate-pulse energies throughout the GaSe crystal for our experimental settings. (b) Linearity figures of merit for varying susceptibilities and MIR pulse energies.

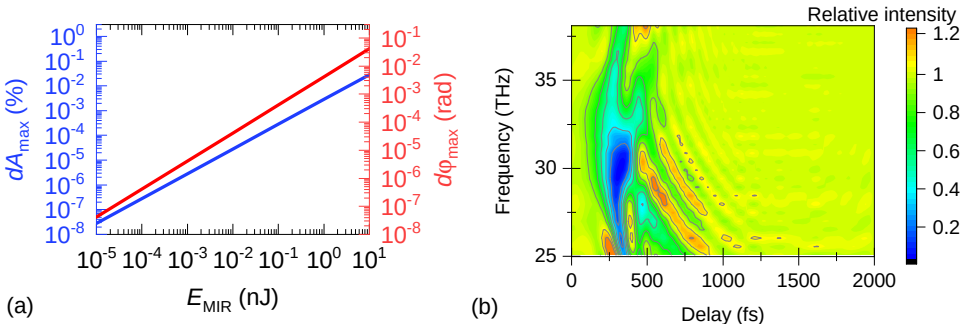

Fig. 10. Geometric scaling example with a gate-pulse energy of 4 μJ, MIR-pulse energy of 10 nJ and a focus size of 350 μm, thus keeping the peak intensities at the crystal the same as in the experiment. (a) Figures of merit for linearity with varying MIR-pulse energy. (b) Simulated spectrally resolved and delay-dependant transmission of the MIR intensity. The global minimum is determined to be 0.039, corresponding to a 96.1% conversion efficiency as compared to 55% in the unscaled case (not shown).

Optics EXPRESS

A.6. Gas sample preparation, signal acquisition, processing, and concentration retrieval

For the preparation of the gas samples, small amounts of the substance were injected into an evacuated ($<10^{-1}$ mbar) gas sampling bulb which was subsequently filled with nitrogen up to atmospheric pressure. Varying amounts of this stock solution were further diluted by injection into a 250-ml syringe filled with nitrogen. In the measurement cell pressure equalization led to a sample pressure of 84 mbar and further dilution. For methanol concentrations higher than 1000 ppm, a flask with liquid methanol was directly connected to the evacuated measurement cell. After removing the remaining gas in the flask with a vacuum pump, the liquid methanol evaporated and the pressure in the gas cell increased until reaching the vapor pressure of 110 mbar @ 19°C. For the 0.5% concentration measurement, the pressure was reduced via repeated pressure equalization with an evacuated cell. For ease of comparison, the specified gas concentrations are given with respect to atmospheric pressure. For the samples used here, the signal strengths at our spectral resolution differ only by ~14% when changing the total pressure from 84 mbar to 1 bar.

For each concentration, ten 10.6-ps-long EOS scans were averaged, each with a measurement time of 8 s. In order to circumvent the dynamic range limitations stemming from the utilized lock-in amplifier (MFLI, Zurich Instruments) and analog-to-digital converter (Picoscale, Smaract), ten additional scans with 100 times higher amplification of the transimpedance amplifier (DLPCA-200, FEMTO) were measured for the weak signals after the main pulse. The two averaged scans were serially stitched at a time delay where the amplified scan was not saturated (typically starting around 1.5 ps). We refer to the result of this procedure as *one trace*. Thus, the effective measurement time of one trace is 80 s. Stitching can, in principle, be avoided by employing electronics with sufficient bit depths (26-bit) or fast scanning techniques (smaller integration time). In order to show the relevant signal and noise of the time-domain EOS traces, their envelopes presented in Fig. 5 were frequency-filtered with a cosine-squared filter, suppressing noise outside the spectral region of the excitation (500-1500 cm^{-1}). The traces were scaled to the mean of the detection noise (single trace, MIR blocked). In the following analysis, a reference trace (evacuated gas cell) was subtracted. For further isolation of the molecular signal from the excitation noise [14], a cosine-squared filter was applied in the time domain (3-9.8 ps). After padding the time-domain traces with zeros up to a delay of 100 ps, they were Fourier transformed. The real-valued magnitude is normalized to the detection noise floor derived from a trace with the MIR beam being blocked (that is, the time-domain SDNR).

For quantitative concentration retrieval using a time-filtering approach, we employed the line-by-line database from HITRAN to calculate the complex attenuation coefficient that includes the effects of temperature and pressure. The HITRAN Application Programming Interface (HAPI) [40] provides for each absorption line i the parameters for a Lorentzian lineshape, namely the line strength (S_i), wavenumber (ν_i) and line width ($\Delta\nu_i$). Under the assumption of a small attenuation, these lines were used to retrieve the lower concentration values. The assumption of a small attenuation breaks down for concentrations >1000 ppm. In order to ensure that we measure only the linear molecular response the measurements were repeated at a hundred times lower MIR power. Differences in the excitation (spectrum and intensity) were corrected using a calculated transfer function and applying it to the trace measured at low power. The resulting spectra of the time filtered traces are in good agreement with the high-power data, confirming a linear measurement of the refractive index of the sample.

A.7. Technical limitations of the detection efficiency

The MIR focus size was chosen for optimum spatial overlap with the gate beam [37]. For a constant detection efficiency and integration time window, i.e. the same required minimum MIR photon flux per second, the minimum detectable field strength scales as follows: Increasing both the MIR and gate beam foci in the EOS crystal by a factor of 2 (to ensure spatial overlap) halves the minimum detectable field strength. Still achieving the same conversion efficiency, would require an increase in gate pulse power by a factor of 4.

Optics EXPRESS

In our experiment, the spectral filter was empirically optimized for the best SDNR, while the theoretical optimum cut-off wavelength [28] would be at approximately 1700nm. This would enable transmission of more than 90% of the generated sum-frequency photons. Increased intensity noise and diode saturation for higher local oscillator power/broader spectral ranges prevented us from balancing to the shot noise limit with such filtering. Overcoming these limitations of purely technical nature would enable a peak $QE_{\mathrm{eff}}(\nu)$ exceeding 50%.

Funding. European Research Council (101088303); Center for Molecular Fingerprinting (CMF); Deutsche Forschungsgemeinschaft (390713860); State Research Center OPTIMAS; Max Planck School of Photonics; Technology Transfer Program of the Max Planck Society; International Max Planck Research School for Advanced Photon Science (IMPRS-APS); Max Planck-UBC-UTokyo Center for Quantum Materials; China Scholarship Council; Bundesministerium für Bildung und Forschung (13N15742).

Acknowledgments. We thank Alexander Apolonski, Liudmila Voronina, Philipp Sulzer for useful discussions.

Disclosures. The authors declare no conflicts of interest.

Data availability. Data and code underlying the results presented in this paper are not publicly available at this time but may be obtained from the authors upon reasonable request.

References

1. T. P. Butler, D. Gerz, C. Hofer, *et al.*, "Watt-scale 50-MHz source of single-cycle waveform-stable pulses in the molecular fingerprint region," Opt. Lett. **44**(7), 1730–1733 (2019).
2. C. Gaida, M. Gebhardt, T. Heuermann, *et al.*, "Watt-scale super-octave mid-infrared intrapulse difference frequency generation," Light:Sci. Appl. **7**(1), 94 (2018).
3. A. Catanese, J. Rutledge, M. C. Silfies, *et al.*, "Mid-infrared frequency comb with 67 W average power based on difference frequency generation," Opt. Lett. **45**(5), 1248–1251 (2020).
4. U. Elu, L. Maidment, L. Vamos, *et al.*, "Seven-octave high-brightness and carrier-envelope-phase-stable light source," Nat. Photonics **15**(4), 277–280 (2021).
5. S. Vasilyev, I. S. Moskalev, V. O. Smolski, *et al.*, "Super-octave longwave mid-infrared coherent transients produced by optical rectification of few-cycle 25-µm pulses," Optica **6**(1), 111–114 (2019).
6. P. Täschler, M. Bertrand, B. Schneider, *et al.*, "Femtosecond pulses from a mid-infrared quantum cascade laser," Nat. Photonics **15**(12), 919–924 (2021).
7. Q. Ru, T. Kawamori, P. G. Schunemann, *et al.*, "Two-octave-wide (3–12 µm) subharmonic produced in a minimally dispersive optical parametric oscillator cavity," Opt. Lett. **46**(4), 709–712 (2021).
8. P. Steinleitner, N. Nagl, M. Kowalczyk, *et al.*, "Single-cycle infrared waveform control," Nat. Photonics **16**(7), 512–518 (2022).
9. A. Sell, R. Scheu, A. Leitenstorfer, *et al.*, "Field-resolved detection of phase-locked infrared transients from a compact Er:fiber system tunable between 55 and 107 THz," Appl. Phys. Lett. **93**(25), 251107 (2008).
10. R. Huber, F. Tauser, A. Brodschelm, *et al.*, "How many-particle interactions develop after ultrafast excitation of an electron–hole plasma," Nature **414**(6861), 286–289 (2001).
11. J. Kröll, J. Darmo, S. S. Dhillon, *et al.*, "Phase-resolved measurements of stimulated emission in a laser," Nature **449**(7163), 698–701 (2007).
12. O. Schubert, M. Hohenleutner, F. Langer, *et al.*, "Sub-cycle control of terahertz high-harmonic generation by dynamical Bloch oscillations," Nat. Photonics **8**(2), 119–123 (2014).
13. T. Deckert, J. Allerbeck, T. Kurihara, *et al.*, "Ultrafast multidimensional spectroscopy with field resolution and noncollinear geometry at mid-infrared frequencies," New J. Phys. **24**(2), 023005 (2022).
14. I. Pupeza, M. Huber, M. Trubetskov, *et al.*, "Field-resolved infrared spectroscopy of biological systems," Nature **577**(7788), 52–59 (2020).
15. A. S. Kowligy, H. Timmers, A. J. Lind, *et al.*, "Infrared electric field sampled frequency comb spectroscopy," Sci. Adv. **5**(6), eaaw8794 (2019).
16. M. T. Peschel, M. Högner, T. Buberl, *et al.*, "Sub-optical-cycle light-matter energy transfer in molecular vibrational spectroscopy," Nat. Commun. **13**(1), 5897 (2022).
17. J. Valdmanis and G. Mourou, "Subpicosecond electrooptic sampling: Principles and applications," IEEE J. Quantum Electron. **22**(1), 69–78 (1986).
18. Q. Wu and X. C. Zhang, "Free-space electro-optic sampling of terahertz beams," Appl. Phys. Lett. **67**(24), 3523–3525 (1995).
19. A. Leitenstorfer, S. Hunsche, J. Shah, *et al.*, "Detectors and sources for ultrabroadband electro-optic sampling: Experiment and theory," Appl. Phys. Lett. **74**(11), 1516–1518 (1999).
20. G. Gallot and D. Grischkowsky, "Electro-optic detection of terahertz radiation," J. Opt. Soc. Am. B **16**(8), 1204–1212 (1999).
21. C. Riek, D. V. Seletskiy, A. S. Moskalenko, *et al.*, "Direct sampling of electric-field vacuum fluctuations," Science **350**(6259), 420–423 (2015).
22. P. R. Griffiths and J. A. De Haseth, *Fourier Transform Infrared Spectrometry* (Wiley-Interscience, 2007).

Optics EXPRESS

23. N. R. Newbury, I. Coddington, and W. Swann, "Sensitivity of coherent dual-comb spectroscopy," Opt. Express **18**(8), 7929–7945 (2010).
24. A. Foltynowicz, T. Ban, P. Masłowski, *et al.*, "Quantum-Noise-Limited Optical Frequency Comb Spectroscopy," Phys. Rev. Lett. **107**(23), 233002 (2011).
25. A. Rogalski, "Next decade in infrared detectors," in *Electro-Optical and Infrared Systems: Technology and Applications XIV*, D. A. Huckridge, R. Ebert, and H. Bürsing, eds. (SPIE, 2017), p. 100.
26. D. M. B. Lesko, H. Timmers, S. Xing, *et al.*, "A six-octave optical frequency comb from a scalable few-cycle erbium fibre laser," Nat. Photonics **15**(4), 281–286 (2021).
27. D. Konnov, A. Muraviev, S. Vasilyev, *et al.*, "High-resolution frequency-comb spectroscopy with electro-optic sampling and instantaneous octave-wide coverage across mid-IR to THz at a video rate," APL Photonics **8**(11), 110801 (2023).
28. M. Porer, J.-M. Ménard, and R. Huber, "Shot noise reduced terahertz detection via spectrally postfiltered electro-optic sampling," Opt. Lett. **39**(8), 2435–2438 (2014).
29. C. Hofer, D. Gerz, M. Högner, *et al.*, "Mid-infrared electric field sampling approaching single-photon sensitivity," EPJ Web Conf. **243**, 16001 (2020).
30. P. Sulzer, K. Oguchi, J. Huster, *et al.*, "Determination of the electric field and its Hilbert transform in femtosecond electro-optic sampling," Phys. Rev. A **101**(3), 033821 (2020).
31. C. Kübler, R. Huber, S. Tübel, *et al.*, "Ultrabroadband detection of multi-terahertz field transients with GaSe electro-optic sensors: Approaching the near infrared," Appl. Phys. Lett. **85**(16), 3360–3362 (2004).
32. K. Liu, J. Xu, and X.-C. Zhang, "GaSe crystals for broadband terahertz wave detection," Appl. Phys. Lett. **85**(6), 863–865 (2004).
33. C. Hofer, D. Gerz, M. Gebhardt, *et al.*, "Electro-Optic Sampling with Percent-Level Detection Efficiency," in *Conference on Lasers and Electro-Optics Europe & European Quantum Electronics Conference* (IEEE, 2021), pp. 1.
34. P. C. D. Hobbs, "Ultrasensitive laser measurements without tears," Appl. Opt. **36**(4), 903–920 (1997).
35. F. D. J. Brunner, J. A. Johnson, S. Grübel, *et al.*, "Distortion-free enhancement of terahertz signals measured by electro-optic sampling I Theory," J. Opt. Soc. Am. B **31**(4), 904–910 (2014).
36. J. A. Johnson, F. D. J. Brunner, S. Grübel, *et al.*, "Distortion-free enhancement of terahertz signals measured by electro-optic sampling II Experiment," J. Opt. Soc. Am. B **31**(5), 1035–1040 (2014).
37. A. Tomasino, A. Parisi, S. Stivala, *et al.*, "Wideband THz Time Domain Spectroscopy based on Optical Rectification and Electro-Optic Sampling," Sci. Rep. **3**(1), 3116 (2013).
38. T. L. Myers, R. G. Tonkyn, T. O. Danby, *et al.*, "Accurate Measurement of the Optical Constants n and k for a Series of 57 Inorganic and Organic Liquids for Optical Modeling and Detection," Appl. Spectrosc. **72**(4), 535–550 (2018).
39. I. E. Gordon, L. S. Rothman, R. J. Hargreaves, *et al.*, "The HITRAN2020 molecular spectroscopic database," J. Quant. Spectrosc. Radiat. Transfer **277**, 107949 (2022).
40. R. V. Kochanov, I. E. Gordon, L. S. Rothman, *et al.*, "HITRAN Application Programming Interface (HAPI): A comprehensive approach to working with spectroscopic data," J. Quant. Spectrosc. Radiat. Transfer **177**, 15–30 (2016).
41. A. V. Muraviev, V. O. Smolski, Z. E. Loparo, *et al.*, "Massively parallel sensing of trace molecules and their isotopologues with broadband subharmonic mid-infrared frequency combs," Nat. Photonics **12**(4), 209–214 (2018).
42. G. Gagliardi and H.-P. Loock, eds., *Cavity-Enhanced Spectroscopy and Sensing* (Springer Berlin Heidelberg, 2014), 179.
43. G. Winkler, L. W. Perner, G.-W. Truong, *et al.*, "Mid-infrared interference coatings with excess optical loss below 10 ppm," Optica **8**(5), 686–696 (2021).
44. P. Sulzer, M. Högner, A.-K. Raab, *et al.*, "Cavity-enhanced field-resolved spectroscopy," Nat. Photonics **16**(10), 692–697 (2022).
45. W. M. Ahmed, O. Lawal, T. M. Nijsen, *et al.*, "Exhaled Volatile Organic Compounds of Infection: A Systematic Review," ACS Infect. Dis. **3**(10), 695–710 (2017).
46. P. Kwee, B. Willke, and K. Danzmann, "New concepts and results in laser power stabilization," Appl. Phys. B **102**(3), 515–522 (2011).
47. D. Gerz, W. Schweinberger, T. P. Butler, *et al.*, "Mid-infrared long-pass filter for high-power applications based on grating diffraction," Opt. Lett. **44**(12), 3014–3017 (2019).
48. N. Karpowicz, "Open source, heterogeneous, nonlinear optics simulation," Opt. Continuum **2**(11), 2244–2254 (2023).
49. K. Kato and N. Umemura, "Sellmeier equations for GaS and GaSe and their applications to the nonlinear optics in GaS_xSe_{1-x}," Opt. Lett. **36**(5), 746–747 (2011).
50. V. G. Dmitriev, G. G. Gurzadyan, and D. N. Nikogosyan, "Properties of Nonlinear Optical Crystals," in *Handbook of Nonlinear Optical Crystals* (Springer Berlin Heidelberg, 1999), 64, pp. 67–288.
51. T. Kawamori, P. G. Schunemann, and K. L. Vodopyanov, "High-order mid-IR multiphoton absorption and nonlinear refraction in GaP, ZnSe, GaSe, and ZGP crystals," in *Conference on Lasers and Electro-Optics* (Optica Publishing Group, 2021), paper STu4C.1.